ADVANCED ENERGY MATERIALS
www.advenergymat.de

Reversible Electron–Holes on O in P2-type $Na_{0.67}Li_{0.1}Ni_{0.3}Mn_{0.6}O_2$

John-Joseph Marie, Max Jenkins, Jun Chen, Gregory Rees, Veronica Cellorio, Jaewon Choi, Stefano Agrestini, Mirian Garcia-Fernandez, Ke-Jin Zhou, Robert A. House, and Peter G. Bruce**

Achieving reversible O-redox through the formation of electron–holes on O could hold the key to a new generation of high energy density Na-ion cathodes. However, to date, it has only been demonstrated in a small handful of cathode materials and none of these materials exploit the dual benefit of high voltage transition metal redox and O-redox, instead relying on $Mn^{3+/4+}$ capacity close to 2 V vs Na^+/Na. Here, a new Na-ion cathode exhibiting electron–holes on O is demonstrated, P2-type $Na_{0.67}Li_{0.1}Ni_{0.3}Mn_{0.6}O_2$, which also utilizes the high voltage $Ni^{3+/4+}$ redox couple to deliver the highest reported energy density among this class of compound. By employing a low Li content and avoiding honeycomb ordering within the transition metal layer, it is possible to stabilize the hole states, and the high voltage plateau is preserved in $Na_{0.67}Li_{0.1}Ni_{0.3}Mn_{0.6}O_2$ over cycling.

1. Introduction

Conventional Na-ion cathode materials store charge through oxidation and reduction of the transition metal ions, i.e., $Mn^{3+/4+}$ in $NaMnO_2$. Nickel is an attractive choice of transition metal as it offers a high voltage and can undergo multiple oxidation state changes $Ni^{2+/3+/4+}$.[1,2] However, in order to maintain the low-cost advantage of Na-ion batteries, the Ni content must be kept low and ultimately alternative high-voltage redox couples need to be found to replace it.[1,3–5]

Storing charge on the oxide ions in the structure is a promising avenue toward high-voltage Na-ion cathode materials.[2,6,7] However, while O^{2-} is oxidized at a high voltage of ≈4.2 V versus Na^+/Na, the subsequent discharge process often occurs at a much lower voltage giving pronounced voltage hysteresis and a loss of energy density. This voltage hysteresis is understood to arise from the formation of molecular O_2 on charge which is trapped within the structure.[8–11] We recently showed that in $Na_{0.6}Li_{0.2}Mn_{0.8}O_2$ it is possible to suppress the formation of molecular O_2 in favor of delocalized electron–holes on O which enables a more reversible high voltage O-redox plateau.[12] This is due to the ribbon-ordered arrangement of Li and Mn within the transition metal layer which is less susceptible to transition metal migration than honeycomb-ordered arrangements.[8] Such migration is required in order to form nano-voids in the structure that can trap the O_2.

Here, we demonstrate a new Na-ion cathode material exhibiting reversible high voltage O-redox without significant O_2 formation, $Na_{0.67}Li_{0.1}Ni_{0.3}Mn_{0.6}O_2$. By lowering the Li content and selecting a transition metal layer composition that is not conducive to honeycomb ordering, in-plane transition metal migration and O_2 formation are successfully suppressed. Furthermore, $Na_{0.67}Li_{0.1}Ni_{0.3}Mn_{0.6}O_2$ exploits high voltage $Ni^{3+/4+}$ redox which, in combination with reversible O-redox, achieves an energy density of >500 Wh kg^{-1} at the cathode level (150 mAh g^{-1} at an average voltage of 3.38 V).

2. Results

$Na_{0.67}Li_{0.1}Ni_{0.3}Mn_{0.6}O_2$ was synthesized by solid-state reaction as described in the Experimental Section. Rietveld refinement of the resulting PXRD data confirms the structure is P2-type (**Figure 1a**; Table S1, Supporting Information). A small amount of unreacted NiO impurity remains in the sample (1.3 wt.% from Rietveld Refinement). A single additional peak is present in the powder X-ray Diffraction (PXRD) pattern at 2θ = 18.3° which

J.-J. Marie, M. Jenkins, J. Chen, G. Rees, R. A. House, P. G. Bruce
Department of Materials
University of Oxford
Parks Road, Oxford OX1 3PH, UK
E-mail: robert.house@materials.ox.ac.uk;
peter.bruce@materials.ox.ac.uk

J.-J. Marie, M. Jenkins, J. Chen, G. Rees, R. A. House, P. G. Bruce
The Faraday Institution
Didcot OX11 0RA, UK

V. Cellorio, J. Choi, S. Agrestini, M. Garcia-Fernandez, K.-J. Zhou
Diamond Light Source
Harwell OX11 0DE, UK

P. G. Bruce
Department of Chemistry
University of Oxford
South Parks Road, Oxford OX1 3TA, UK

The ORCID identification number(s) for the author(s) of this article can be found under https://doi.org/10.1002/aenm.202401935

DOI: 10.1002/aenm.202401935

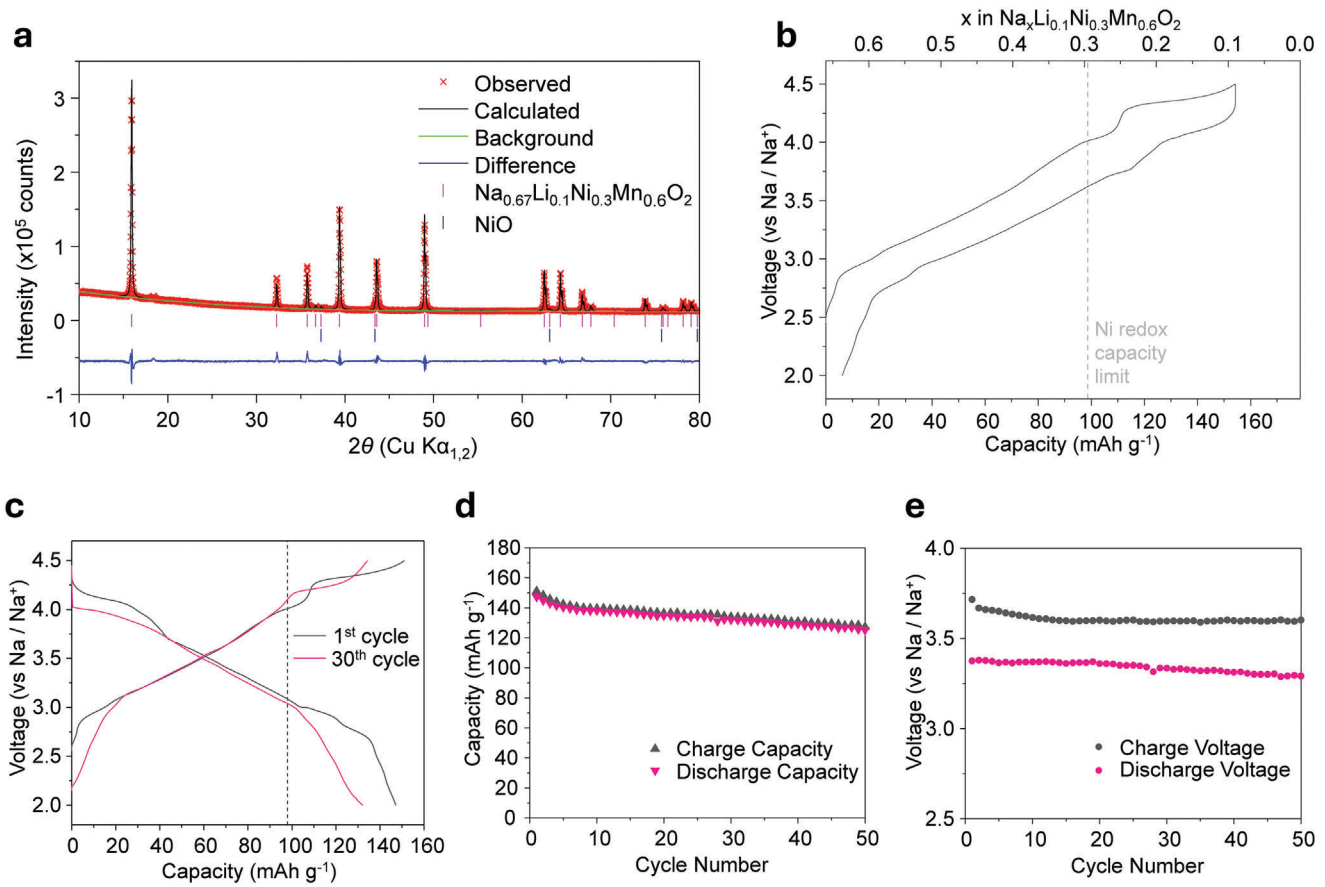

Figure 1. Structure and electrochemistry of P2-type $Na_{0.67}Li_{0.1}Ni_{0.3}Mn_{0.6}O_2$. a) PXRD and refinement of pristine material with 1.3 wt.% NiO impurity. b) first cycle load curve versus Na metal at 10 mA g^{-1} charged to 4.5 V. c) 1st and 30th cycle load curves. d) capacity retention over cycles 1–50. e) average voltage on charge and discharge over cycles 1–50. All data were collected at 10 mA g^{-1} between voltage limits of 2 and 4.5 V.

cannot be indexed to either honeycomb ordering in the transition metal (TM) layer or to a Li_2MnO_3 impurity. It is possible this arises from an unidentified in-plane ordering scheme between Li and Ni/Mn. Scanning Electron Microscopy (SEM) images reveal a plate-like morphology, with a particle size of 1–2 µm. Energy dispersive X-ray spectroscopy (EDX) reveals a homogenous distribution of elements within the particles (Figure S1, Supporting Information). The material composition was also verified via inductively coupled plasma - optical emission spectroscopy (ICP-OES) analysis (Table S2, Supporting Information).

The first cycle load curve of $Na_{0.67}Li_{0.1}Ni_{0.3}Mn_{0.6}O_2$ is shown in Figure 1b. On charge, the material shows a long sloping region up to 4 V; the associated capacity corresponds to the charge required to oxidize $Ni^{2.8+}$ to Ni^{4+}. Beyond this, just over 0.2 mol of Na is extracted across a high-voltage plateau. On discharge, a significant proportion of plateau capacity is returned above 4 V before turning to a steady sloping region down to 2 V. Operando electrochemical mass spectrometry, OEMS, rules out any significant loss of O through either CO_2 or O_2 release over the first cycle (Figure S2, Supporting Information). The lack of CO_2, which is often seen in Na-ion cathodes, indicates that minimal carbonate contaminants are present on the surface of our material and that the extent of electrolyte decomposition from reactive oxygen species is also small.

Over cycling, the high voltage plateau on charge and discharge persists with a slight decrease in the average voltage, Figure 1c. Some fading in the capacity and voltage is observed, but to a much lesser extent than other O-redox cathodes, Figure 1d,e.[8,13]

In order to understand the structural changes occurring over the 1st cycle, operando PXRD was carried out. On charge, the material shows a continuous shift of the 002 peak towards lower 2θ values which corresponds to an increase in the inter-layer spacing from 5.52 to 5.67 Å, **Figures** 2a and S3 (Supporting Information). At the beginning of the high voltage plateau, a phase change is observed from P2- to OP4-type stacking.[14] On discharge, the material reverts to P2-type stacking with similar lattice parameters to the pristine material. P to O phase transitions are often accompanied by a degree of voltage hysteresis even in the absence of oxygen redox,[14–16] offering an explanation for the difference in charge and discharge potential of the high voltage plateau observed here for $Na_{0.67}Li_{0.1}Ni_{0.3}Mn_{0.6}O_2$.

The corresponding changes to the local environment of the Na and Li accompanying this structural transition were followed by solid state ^{23}Na and ^{7}Li nuclear magnetic resonance (NMR) spectroscopy. The ^{23}Na NMR, Figure 2b, shows one Na environment corresponding to Na in the alkali metal (AM) layer (in purple). The signal shifts from 1570 ppm in the pristine sample to

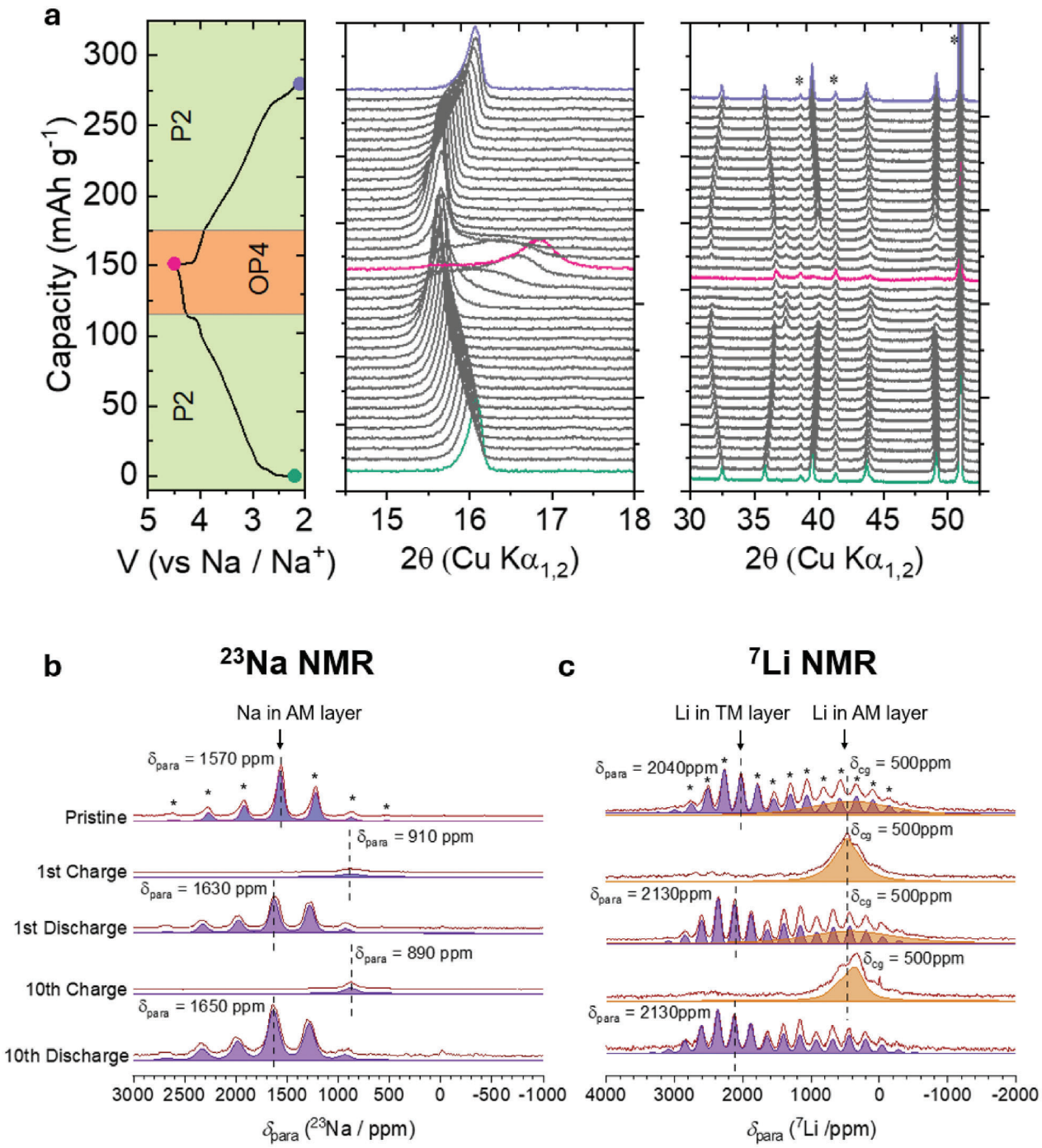

Figure 2. Structural evolution of $Na_{0.67}Li_{0.1}Ni_{0.3}Mn_{0.6}O_2$. a) Operando X-ray diffraction. $Na_{0.67}Li_{0.1}Ni_{0.3}Mn_{0.6}O_2$ undergoes a reversible P2-OP4 phase transition across the high voltage plateau. * denotes peaks from cell components. b) Solid state ^{23}Na NMR. Na is removed and reinserted into prismatic Na sites in the alkali metal (AM) layer (purple) during charge and discharge. c) Solid state ^{7}Li NMR. Li occupies ordered sites within the TM layer (purple) and migrates reversibly into O-type sites in the Na layer on charge (orange). Ordered Li sites within the TM layer are retained after 10 cycles. * denotes spinning sidebands.

910 ppm in the charged sample in line with the oxidation of paramagnetic Ni^{3+} to Ni^{4+} which is diamagnetic. The ^{23}Na signal becomes paramagnetically shifted again on discharge to 1630 ppm as Ni^{4+} is reduced. Over the 10th charge/discharge cycle, the ^{23}Na signal shows a similar range of shifts from 890 ppm on charge to 1650 ppm on discharge. The differences in shift for these environments before and after cycling are difficult to resolve due to the broad, featureless nature of the peaks and the low signal intensity, particularly in charged samples from which most of the Na has been removed.

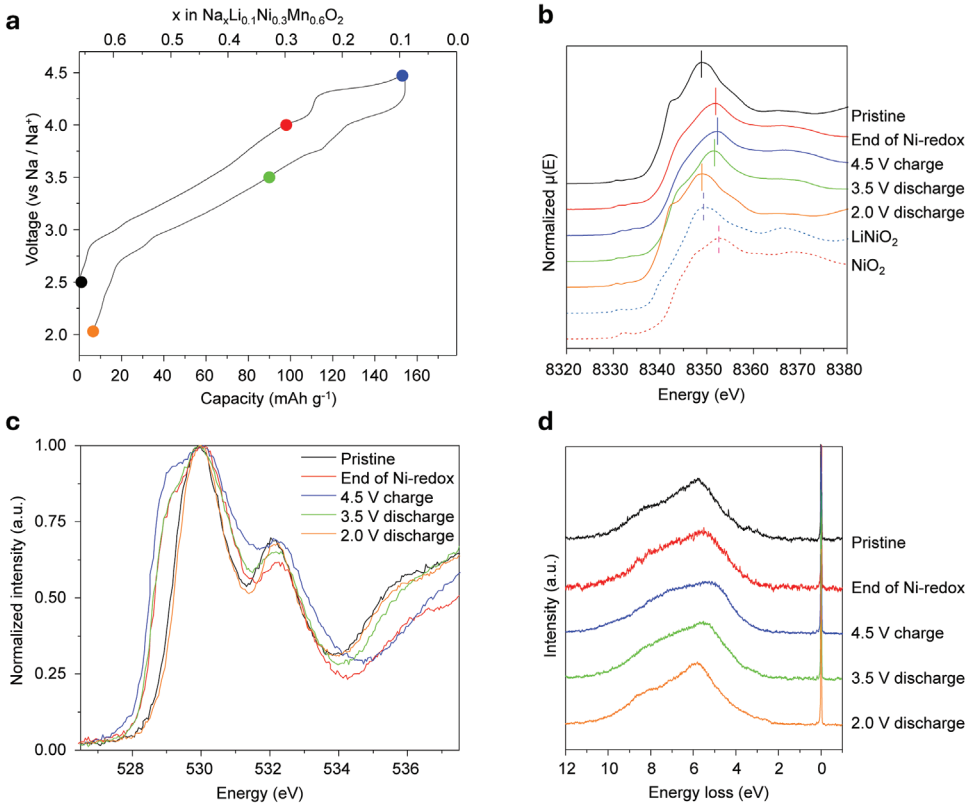

Figure 3. Ni and O spectroscopies for $Na_{0.67}Li_{0.1}Ni_{0.3}Mn_{0.6}O_2$ over the first cycle a) Load curve for $Na_{0.67}Li_{0.1}Ni_{0.3}Mn_{0.6}O_2$ with states of charge chosen for ex situ analysis. b) Ni K-edge XANES. Ni oxidizes from +2.8 in the pristine state to +4 by $Na_{0.3}$. There is little further change in the edge position across the high voltage plateau on charge or until re-sodiating beyond $Na_{0.3}$ on discharge c) O K-edge XAS spectra. An increase in the leading edge of the pre-edge up to $Na_{0.3}$ on charge is consistent with Ni oxidation to Ni^{4+}. Beyond $Na_{0.3}$, the intensity in this region continues to increase despite no further Ni oxidation indicating the formation of electron–holes on O. d) O K-edge RIXS at 531.5 eV, the resonant energy for molecular O_2. No evidence of molecular O_2 formation is observed over the entire first cycle.

Turning to the ^{7}Li NMR, Figure 2c, two distinct Li environments are observed in the pristine material. The main environment centred at a chemical shift of 2060 ppm (in purple) can be attributed to Li in the TM layer, being paramagnetically shifted due to Mn^{4+} present in the layer. The second environment (in orange) is attributed to Li in octahedral sites within AM layers that are O-type stacking faults in the structure. The presence of these two distinct environments is confirmed by projected magic-angle tuning phase adjusted spinning sidebands (pj-MATPASS) experiments in Figure S4 (Supporting Information). The strength of paramagnetic interactions experienced by Na are greater than Li due to the larger number of electrons around the Na-ion, hence the chemical shifts are higher for Na and the differences are more pronounced. At the end of the 1st charge, a single broad ^{7}Li signal at 500 ppm is observed indicating Li migration from the TM layer into the AM layer in octahedral sites in the OP4 structure. On the 1st discharge, the sharp ^{7}Li signal for Li in the TM layer reappears as the structure returns to P2-type stacking. Similar changes are observed on the 10th cycle and in the 10th discharged state, the sharpness of the Li signal remains indicating a similar degree of ordering to the pristine material is retained in the TM layer.

To investigate the charge compensation mechanism in $Na_{0.67}Li_{0.1}Ni_{0.3}Mn_{0.6}O_2$, ex situ X-ray absorption spectroscopy (XAS) and X-ray absorption near-edge structure (XANES) measurements of the O K-edge and Ni, Mn K-edges were collected over the first cycle, **Figure 3**a. The Ni K-edge position for the pristine material is slightly lower in energy than the edge position for Ni^{3+} in $LiNiO_2$, consistent with the nominal $Ni^{2.8+}$ oxidation state according to its composition. On charging to 4 V, the edge shifts close to that of Ni^{4+} in charged $LiNiO_2$. This state of charge corresponds to a Na content of 0.3 and a composition implying both Ni and Mn in the +4 oxidation state, Figure 3b. Between 4and 4.5 V there is no significant further Ni oxidation observed, despite 0.2 further moles of Na removal. The white line energies for these states of charge are in good agreement with the measured Ni^{4+} reference. On discharge, the majority of Ni reduction occurs when re-sodiating beyond a Na content of 0.3, and by 2 V, the Ni edge has returned to a similar energy to that of the pristine. In contrast, the Mn K-edge remains unchanged throughout the first cycle, Figure S5 (Supporting Information). The O K-edge shows an increase in the pre-edge intensity between the pristine and 4 V states of charge which is consistent with removal of electrons from hybridised Ni3d-O2p orbitals, corresponding to Ni oxidation from +2.8 to +4, Figure 3c. Charging beyond 4 to 4.5 V, a further increase in the pre-edge intensity is observed, which cannot be attributed to Ni oxidation given the lack of significant change in the Ni XANES. This must therefore signify the formation of electron–hole states

on the oxide sub-lattice. The feature arising from the formation of electron–holes in $Na_{0.67}Li_{0.1}Ni_{0.3}Mn_{0.6}O_2$ (528–529 eV) is consistent with previous measurements of electron–holes in Na-ion O-redox cathodes. Given the shift of the Ni K-edge before 4 V and lack of further significant change during the high voltage region, we conclude that Ni and O oxidation are separate processes. On discharge, the increase in pre-edge intensity is reversed, with the spectrum at 2 V looking identical to that of the pristine material.

To investigate the possible formation of O—O species in the bulk after O oxidation, we employed high-resolution O K-edge resonant inelastic X-ray scattering (RIXS). While other techniques, such as electron paramagnetic resonance (EPR)[17–19] or X-ray photoelectron spectroscopy (XPS),[20,21] have been deployed to probe the nature of O—O species in O—redox cathodes, the benefit of high-resolution RIXS is its ability to distinguish O-O species of different bond lengths by measuring the characteristic spacing between vibrational energy levels. Using RIXS, it has been possible to identify the presence of molecular O_2 trapped within a wide range of battery cathode materials, as well as superoxide ($O_2^- = 1.34$ A), and peroxide species ($O_2^{2-} = 1.49$ A) in reference compounds. Note that it is important to carry out the RIXS measurements using the correct protocols to avoid beam damage that can lead to erroneous results. Importantly, our RIXS collected results here for $Na_{0.67}Li_{0.1}Ni_{0.3}Mn_{0.6}O_2$, show no evidence of O_2 formation over the 1st charge, or other O—O species. These results confirm that Na extraction from $Na_{0.67}Li_{0.1}Ni_{0.3}Mn_{0.6}O_2$ is charge compensated by sequential Ni-redox and formation of electron–holes on O, as opposed to trapped O_2.

To probe the reversibility of the Ni- and O-redox charge compensation mechanisms with cycling, RIXS, XAS, and XANES were employed. O K-edge RIXS shows an increase in signal arising from trapped molecular O_2 in the material in the fully charged state. Despite this, the feature corresponding to electron–hole states on O in the O XAS remains intense after 30 cycles, **Figure 4c**, indicating that reversible O-redox is still the dominant O-redox charge compensation mechanism. The Ni K-edge XANES, Figure 4e,f, show consistent oxidation and reduction of Ni over 30 cycles without evidence of significant over-reduction on discharge and there is no change in the Mn K-edge, Figure S5 (Supporting Information).

3. Discussion

Reversible, high voltage oxygen redox involving the formation of electron–holes on O, has only been observed in a limited number of materials to date, such as P2- and P3-type $Na_{0.6}Li_{0.2}Mn_{0.8}O_2$[8,12,13,22–25] and $Na_2Mn_3O_7$.[26–29] The suppression of transition metal migration is critical to avoiding voltage hysteresis by preventing the formation of trapped O_2 and preserving electron–holes on O. We previously showed that in-plane ordering of Li within the transition metal layer is an important factor suppressing transition metal migration. When the Li and TM ions are ordered in a honeycomb arrangement, as in conventional Li-rich cathodes like $Li_{1.2}Ni_{0.2}Mn_{0.6}O_2$, as Li leaves the TM layers, reorganization of the TM ions to form vacancy clusters able to accommodate O_2 occurs, enabling the formation of trapped O_2. In this case, only a few in-plane transition metal migration events are required before vacancy clusters large enough to accommodate O_2 are formed.[8] In contrast, in the ribbon and mesh-ordered structures, more migration events are required as the transition metal vacancies are spaced further apart. Here, in $Na_{0.67}Li_{0.1}Ni_{0.3}Mn_{0.6}O_2$, we employed an even lower Li content than before and a transition metal layer composition not conducive to the honeycomb arrangement through ion size or charge ordering to enable greater suppression of transition metal migration and O_2 formation, **Figure 5**. This strategy affords greater stability to the hole states on oxygen, enabling them to persist for long enough to be observed in ex situ samples and to support stable cycling of the high voltage O-redox plateau. A small amount of voltage hysteresis is observed across the high voltage plateau, consistent with the behaviour of other layered materials which undergo transitions from P-type to O-type stacking at high degrees of desodiation.

While others have previously reported similar compositions to the one studied here,[17,31–34] we are the first to show that P2-type $Na_{0.67}Li_{0.1}Ni_{0.3}Mn_{0.6}O_2$ exhibits excess capacity supported by hole states on O, expanding the number of known reversible O-redox cathodes. It has been previously claimed that the suppression of voltage hysteresis in these compounds arises from the inclusion of Ni.[31] We show it is due to the lack of honeycomb ordering in $Na_{0.67}Li_{0.1}Ni_{0.3}Mn_{0.6}O_2$, due to the suppression of in-plane transition metal migration which prevents the formation of trapped O_2, favoring stable hole states on O. Furthermore, in addition to the reversible O-redox couple, this material also exploits the high voltage $Ni^{3+/4+}$ redox couple. With an average discharge voltage of 3.4 V and capacity of 150 mAh g^{-1}, $Na_{0.67}Li_{0.1}Ni_{0.3}Mn_{0.6}O_2$ offers the highest energy density (≈500 Wh kg^{-1}) of known materials exploiting O-redox through the creation of hole states on O, **Figure 6**. We anticipate that materials modifications such as pre-sodiation of the cathode to enable greater utilization of the available Na sites in the Na layer will lead to further improvements in energy density.

4. Conclusion

We have demonstrated a new Na-ion cathode exhibiting a reversible O-redox plateau supported by electron–holes on O and with suppressed O_2 formation. This material is the first reversible O-redox cathode which also exploits high voltage transition metal redox to deliver competitive energy density ≈500 Wh kg^{-1} at the cathode level. Upon desodiating P2-type $Na_{0.67}Li_{0.1}Ni_{0.3}Mn_{0.6}O_2$ to a sodium content of 0.3, Ni is oxidized from +2.8 to +4. Beyond this, a further 0.2 moles of sodium can be extracted generating electron–hole states on O seen as an increase in the pre-edge of the O K-edge XAS and a lack of trapped O_2 by RIXS. This process is reversed on discharge and the dual Ni- and O-redox couples can be cycled for up to 30 cycles with only minor voltage fade. This material marks an important milestone towards viable O-redox cathodes for Na-ion batteries.

5. Experimental Section

Synthesis: $Na_{0.67}Li_{0.1}Ni_{0.3}Mn_{0.6}O_2$ was synthesized via the solid-state method. Stoichiometric amounts of $NaNO_3$ (>99%, Sigma), $LiNO_3$ (>99%, Sigma), $NiCO_3$ (98%, Alfa), and $MnCO_3$ (99.9%, Alfa) were mixed in a planetary ball-mill for 2 h. The precursors were then pressed

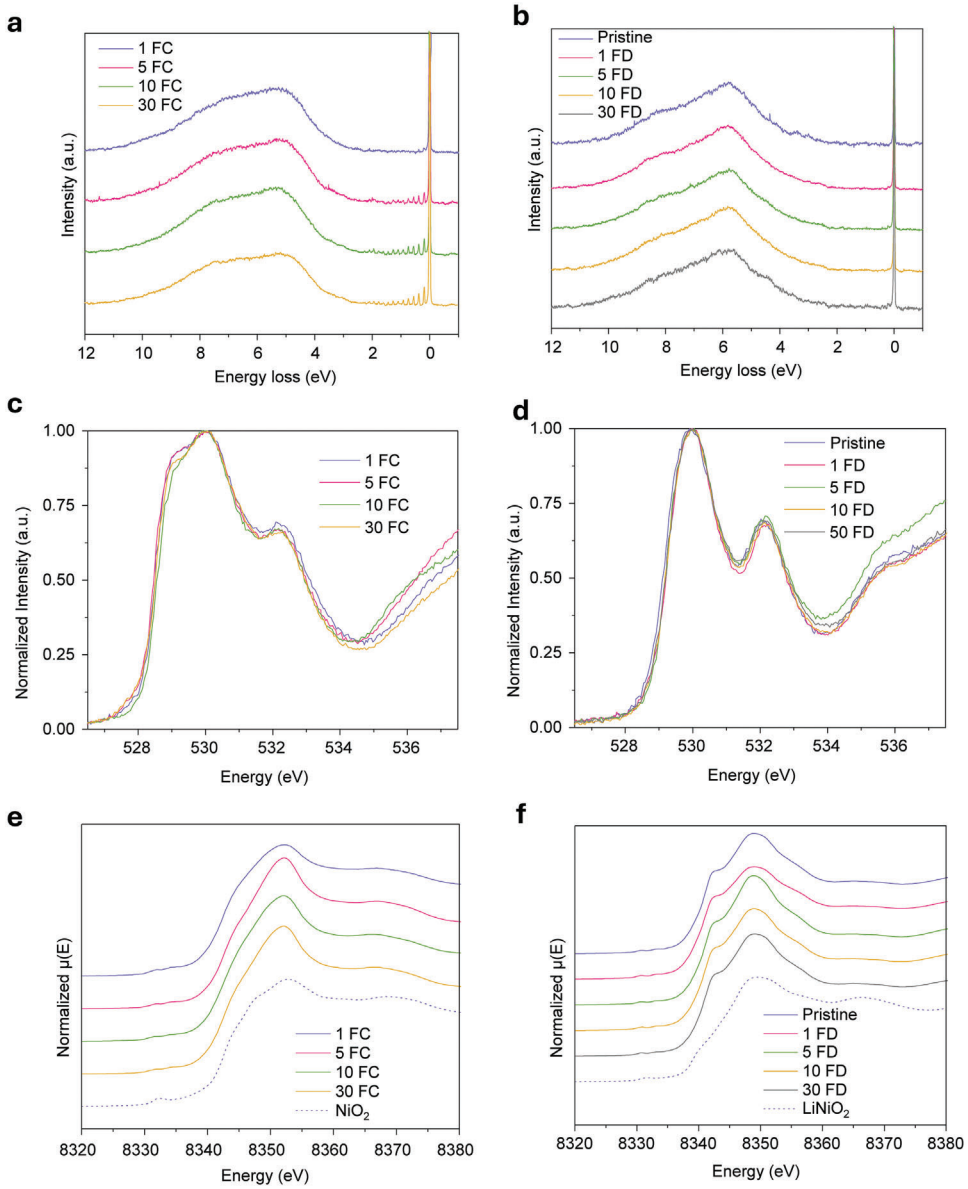

Figure 4. Ni and O spectroscopies for $Na_{0.67}Li_{0.1}Ni_{0.3}Mn_{0.6}O_2$ over the first 30 cycles. a,b) O K-edge RIXS at 531.5 eV, the resonance energy of trapped O_2, on charge and discharge respectively. Minor amounts of O_2 emerge on charge over cycling. c,d) O K-edge XAS, on charge and discharge respectively. The intensity of the pre-edge feature arising from holes states on O is well-maintained on charge over cycling. e) and f Ni K-edge XANES on charge and discharge respectively. Ni continues to cycle reversibly between +2.8 and +4 without evidence of significant over-reduction.

into pellets and heated to 800 °C for 8 h under flowing O_2. A heating rate of 3 °C min^{-1} was used, and the furnace was left to cool naturally after the synthesis.

Electrochemistry: Electrode preparations and cell (dis)assembly were performed in a glove box under an inert argon atmosphere (H_2O <0.1 ppm and O_2 <0.1 ppm). Electrodes were prepared by combining the active material (80wt%) and Super P carbon (10 wt.%) in a mortar and pestle before adding PTFE binder (10 wt.%). The electrode film was then rolled to a thickness of ≈100 µm. Electrodes were assembled into coin cells using glass fibre separators and 1 M $NaClO_4$ in PC with 5% FEC (99.9%, DodoChem), and a Na metal counter electrode. Galvanostatic cycling was carried out using a Maccor Series 4000. Cycling was performed between 2.0 and 4.5 V versus Na^+/Na at a rate of 20 mA g^{-1} for all cells for all samples unless stated otherwise. Typical mass loadings were 15 mg cm^{-2}

PXRD: Diffraction data were collected on a Rigaku 9 kW SmartLab Cu-source diffractometer equipped with a Hypix 2D detector. Operando PXRD data were collected using an electrochemical cell provided by Rigaku with a beryllium window.

SEM: SEM imaging and EDX analysis were performed on a Carl Zeiss Merlin high-resolution field emission gun SEM instrument.

OEMS: OEMS experiments were carried out by flowing Ar carrier gas (99.9% purity, BOC) through an ECC-std electrochemical cell (EL-CELL) with gas inlet and outlet ports and into a BT Prima mass spectrometer (Thermo Fischer). The cathode material was cycled versus a Na metal counter electrode and an electrolyte of 1 M NaPF6 in PC.

Solid State MAS NMR: All ^{7}Li and ^{23}Na magic angle spinning (MAS, υR = 37 037 Hz) solid-state NMR measurements were completed at 9.45 T (υ07Li = 155.53 MHz, υ023Na = 105.86 MHz) using a Bruker Avance III

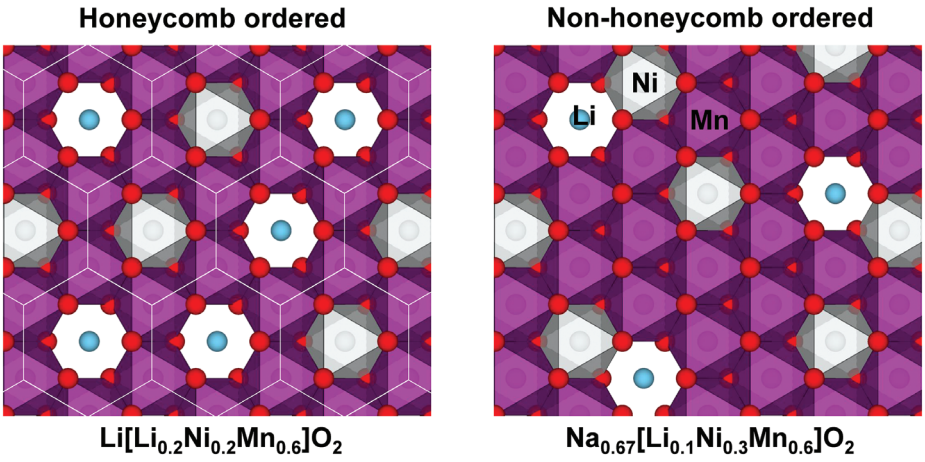

Figure 5. In-plane ordering schemes Li, Ni, and Mn within the transition metal layer occupy a honeycomb arrangement in Li-rich $Li_{1.2}Ni_{0.2}Mn_{0.6}O_2$ and a non-honeycomb arrangement here in $Na_{0.67}[Li_{0.1}Ni_{0.3}Mn_{0.6}]O_2$.

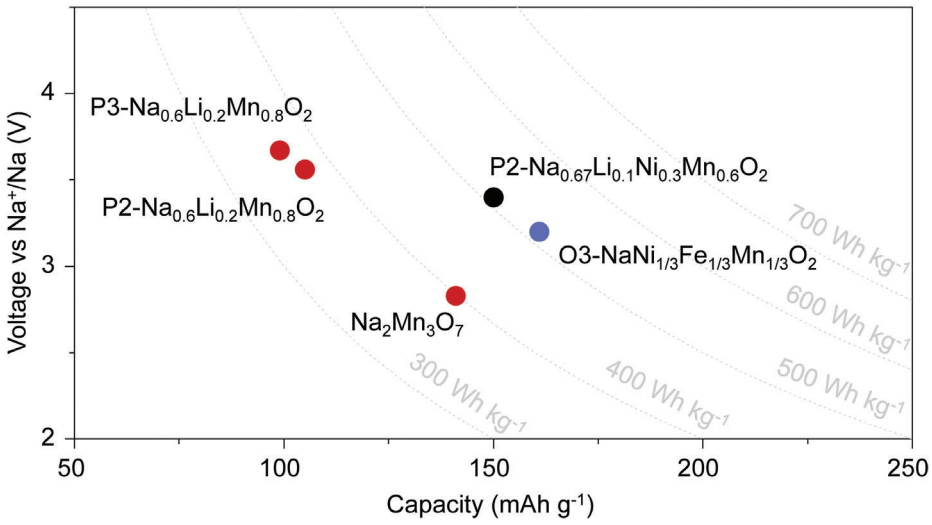

Figure 6. Energy density plot. Average voltage versus capacity for other reported reversible O-redox cathodes P3-$Na_{0.6}Li_{0.2}Mn_{0.8}O_2$,[13] P2-$Na_{0.6}Li_{0.2}Mn_{0.8}O_2$,[13] and $Na_2Mn_3O_7$,[26] (in red) and our compound P2-$Na_{0.67}Li_{0.1}Ni_{0.3}Mn_{0.6}O_2$ (black), between the same voltage limits of 2–4.5 V. A benchmark transition metal redox cathode O3-$NaNi_{1/3}Fe_{1/3}Mn_{1/3}O_2$ is shown in blue between voltage limits of 2–4.3 V.[30]

HD spectrometer and a 1.9 mm double air bearing MAS probe. All ^{7}Li and ^{23}Na spectra were referenced to 1 M LiCl(aq) and 1 M NaCl(aq) in D_2O, respectively, at 0 ppm. All spectra were recorded using a Hahnecho ($\pi/2$-τ-π-τ) sequence. Where τ is $1/\upsilon R$ and $\pi/2$ is 250 kHz, the resultant FID is processed as a half echo. The ^{7}Li spectra were achieved with a recycle delay of 300 ms. The ^{23}Na NMR spectra were collected with relaxation times of 500 ms. The isotropic resonance was determined by varying the spinning speed between 30 and 39 kHz to isolate the spinning sidebands.

ICP-OES: The pristine cathode material was dissolved in aqua regia ($HCl:HNO_3$ / 25:75 (v/v%)) before diluting the solution for measurement. A calibration curve was created using standard solutions of Li, Ni, Mn, and Na. Elemental analysis was carried out using a Perkin–Elmer Optima 7300DV ICP–OES.

RIXS and XAS: High-resolution RIXS data were collected using the I21 beamline at Diamond Light Source.[35] To produce the data sets for the quantitative analysis, scans at 531 eV were recorded at fifteen different sample locations and averaged together, with little inhomogeneity in the signal observed. O K-edge XAS were collected in fluorescence mode using the I21 beamline at Diamond Light Source. Data were averaged across 3 scans.

XANES: Ex situ TM K-edge data were collected at the B18 beamline at Diamond Light Source. These data were collected in transmission mode.

Supporting Information

Supporting Information is available from the Wiley Online Library or from the author.

Acknowledgements

P.G.B. is indebted to the EPSRC, the Henry Royce Institute for Advanced Materials (EP/R00661X/1, EP/S019367/1, EP/R010145/1, and EP/L019469/1), and the Faraday Institution (FIRG016) for financial support. R.A.H. acknowledges funding from the Royal Academy of Engineering under the Research Fellowship scheme. The authors acknowledge Diamond Light Source for beamtime on I21 under proposal MM25785 and for block allocation group (B.A.G.) time on B18.

Conflict of Interest

The authors declare no conflict of interest.

Author Contributions

J.-J.M. conducted the synthesis and characterization work with M.J. J.-J.M., J.C., and V.C. performed the XANES measurements. G.J.R. performed and fitted the MAS NMR. R.A.H. and J.-J.M. in close collaboration with S.A., J.C., M.G.-F. and K.-J.Z. conducted the XAS and RIXS measurements. J.-J.M., R.A.H., and P.G.B. wrote the paper with contributions from all authors.

Data Availability Statement

The data that support the findings of this study are available from the corresponding author upon reasonable request.

Keywords

Cathodes, Na-ion batteries, oxygen redox, RIXS, XAS

Received: May 1, 2024
Revised: July 11, 2024
Published online: July 26, 2024

[1] A. Rudola, A. J. R. Rennie, R. Heap, S. S. Meysami, A. Lowbridge, F. Mazzali, R. Sayers, C. J. Wright, J. Barker, *J. Mater. Chem. A* **2021**, *9*, 8279.
[2] Y. You, A. Manthiram, Y. You, A. Manthiram, *Adv. Energy Mater.* **2018**, *8*, 1701785.
[3] H. S. Hirsh, Y. Li, D. H. S. Tan, M. Zhang, E. Zhao, Y. Shirley Meng, H. S. Hirsh, Y. Li, D. H. S. Tan, M. Zhang, E. Zhao, Y. S. Meng, *Adv. Energy Mater.* **2020**, *10*, 2001274.
[4] C. Vaalma, D. Buchholz, M. Weil, S. Passerini, *Nat. Rev. Mater.* **2018**, *3*, 18013.
[5] N. Tapia-Ruiz, A. R. Armstrong, H. Alptekin, M. A. Amores, H. Au, J. Barker, R. Boston, W. R. Brant, J. M. Brittain, Y. Chen, M. Chhowalla, Y. S. Choi, S. I. R. Costa, M. C. Ribadeneyra, S. A. Cussen, E. J. Cussen, W. I. F. David, A. V. Desai, S. A. M. Dickson, E. I. Eweka, J. D. Forero-Saboya, C. P. Grey, J. M. Griffin, P. Gross, X. Hua, J. T. S. Irvine, P. Johansson, M. O. Jones, M. Karlsmo, E. Kendrick, et al., *J. Phys. Energy.* **2021**, *3*, 031503.
[6] P. Rozier, M. Sathiya, A. R. Paulraj, D. Foix, T. Desaunay, P. L. Taberna, P. Simon, J. M. Tarascon, *Electrochem. Commun.* **2015**, *53*, 29.
[7] B. Mortemard de Boisse, G. Liu, J. Ma, S.-I. Nishimura, S.-C. Chung, H. Kiuchi, Y. Harada, J. Kikkawa, Y. Kobayashi, M. Okubo, A. Yamada, *Nat. Commun.* **2016**, *7*, 11397.
[8] R. A. House, U. Maitra, M. A. Pérez-Osorio, J. G. Lozano, L. Jin, J. W. Somerville, L. C. Duda, A. Nag, A. Walters, K.-J. Zhou, M. R. Roberts, P. G. Bruce, *Nature* **2020**, *577*, 502.
[9] R. A. House, G. J. Rees, M. A. Pérez-Osorio, J. J. Marie, E. Boivin, A. W. Robertson, A. Nag, M. Garcia-Fernandez, K. J. Zhou, P. G. Bruce, *Nat. Energy* **2020**, *5*, 777.
[10] R. A. House, J. J. Marie, M. A. Pérez-Osorio, G. J. Rees, E. Boivin, P. G. Bruce, *Nat. Energy* **2021**, *6*, 781.
[11] E. Boivin, R. A. House, M. A. Pérez-Osorio, J. J. Marie, U. Maitra, G. J. Rees, P. G. Bruce, *Joule* **2021**, *5*, 1267.
[12] R. A. House, G. J. Rees, K. McColl, J. J. Marie, M. Garcia-Fernandez, A. Nag, K. J. Zhou, S. Cassidy, B. J. Morgan, M. Saiful Islam, P. G. Bruce, *Nat. Energy* **2023**, *8*, 351.
[13] A. Gao, Q. Zhang, X. Li, T. Shang, Z. Tang, X. Lu, Y. Luo, J. Ding, W. H. Kan, H. Chen, W. Yin, X. Wang, D. Xiao, D. Su, H. Li, X. Rong, X. Yu, Q. Yu, F. Meng, C. Nan, C. Delmas, L. Chen, Y. S. Hu, L. Gu, *Nat. Sustain.* **2021**, *5*, 214.
[14] J. W. Somerville, A. Sobkowiak, N. Tapia-Ruiz, J. Billaud, J. G. Lozano, R. A. House, L. C. Gallington, T. Ericsson, L. Häggström, M. R. Roberts, U. Maitra, P. G. Bruce, *Energy Environ. Sci.* **2019**, *12*, 2223.
[15] Z. Lu, J. R. Dahn, *J. Electrochem. Soc.* **2001**, *148*, A1225.
[16] N. Yabuuchi, M. Kajiyama, J. Iwatate, H. Nishikawa, S. Hitomi, R. Okuyama, R. Usui, Y. Yamada, S. Komaba, *Nat. Mater.* **2012**, *11*, 512.
[17] Y. Liao, H. Feng, Q. Yang, M. Shen, Y. Jiang, C. Li, C. Zhao, F. Geng, B. Hu, *ACS Appl. Mater. Interfaces* **2023**, *15*, 10709.
[18] C. Zhao, C. Li, H. Liu, Q. Qiu, F. Geng, M. Shen, W. Tong, J. Li, B. Hu, *J. Am Chem. Soc.* **2021**, *143*, 18652.
[19] M. Sathiya, J. B. Leriche, E. Salager, D. Gourier, J. M. Tarascon, H. Vezin, *Nat. Commun.* **2015**, *6*, 6276.
[20] M. Sathiya, G. Rousse, K. Ramesha, C. P. Laisa, H. Vezin, M. T. Sougrati, M.-L. L. Doublet, D. Foix, D. Gonbeau, W. Walker, A. S. Prakash, M. Ben Hassine, L. Dupont, J.-M. M. Tarascon, *Nat. Mater.* **2013**, *12*, 827.
[21] G. Assat, D. Foix, C. Delacourt, A. Iadecola, R. Dedryvère, J. M. Tarascon, *Nat. Commun.* **2017**, *8*, 2219.
[22] K. Du, J. Zhu, G. Hu, H. Gao, Y. Li, J. B. Goodenough, *Energy Environ. Sci.* **2016**, *9*, 2575.
[23] X. Rong, J. Liu, E. Hu, Y. Liu, Y. Wang, J. Wu, X. Yu, K. Page, Y. S. Hu, W. Yang, H. Li, X. Q. Yang, L. Chen, X. Huang, *Joule* **2018**, *2*, 125.
[24] E. J. Kim, P. A. Maughan, E. N. Bassey, R. J. Clément, L. A. Ma, L. C. Duda, D. Sehrawat, R. Younesi, N. Sharma, C. P. Grey, A. R. Armstrong, *Adv. Energy Mater.* **2022**, *12*, 2102325.
[25] D. Eum, B. Kim, J. H. Song, H. Park, H. Y. Jang, S. J. Kim, S. P. Cho, M. H. Lee, J. H. Heo, J. Park, Y. Ko, S. K. Park, J. Kim, K. Oh, D. H. Kim, S. J. Kang, K. Kang, *Nat. Mater.* **2022**, *21*, 664.
[26] B. Mortemard de Boisse, S. ichi Nishimura, E. Watanabe, L. Lander, A. Tsuchimoto, J. Kikkawa, E. Kobayashi, D. Asakura, M. Okubo, A. Yamada, *Adv. Energy Mater.* **2018**, *8*, 1800409.
[27] I. I. Abate, C. Das Pemmaraju, S. Y. Kim, K. H. Hsu, S. Sainio, B. Moritz, J. Vinson, M. F. Toney, W. Yang, W. E. Gent, T. P. Devereaux, L. F. Nazar, W. C. Chueh, *Energy Environ. Sci.* **2021**, *14*, 4858.
[28] B. Song, M. Tang, E. Hu, O. J. Borkiewicz, K. M. Wiaderek, Y. Zhang, N. D. Phillip, X. Liu, Z. Shadike, C. Li, L. Song, Y. Y. Hu, M. Chi, G. M. Veith, X. Q. Yang, J. Liu, J. Nanda, K. Page, A. Huq, *Chem. Mater.* **2019**, *31*, 3756.
[29] A. Tsuchimoto, X. M. Shi, K. Kawai, B. Mortemard de Boisse, J. Kikkawa, D. Asakura, M. Okubo, A. Yamada, *Nat. Commun.* **2021**, *12*, 631.
[30] Y. Xie, H. Wang, G. Xu, J. Wang, H. Sheng, Z. Chen, Y. Ren, C.-J. Sun, J. Wen, J. Wang, D. J. Miller, J. Lu, K. Amine, Z.-F. Ma, Y. Xie, H. Wang, Z. Ma, G. Xu, Z. Chen, J. Lu, K. Amine, J. Wang, H. Sheng, J. G. Wen, D. J. Miller, Y. Ren, C. Sun, *Adv. Energy Mater.* **2016**, *6*, 1601306.
[31] N. Voronina, M. Y. Shin, H. J. Kim, N. Yaqoob, O. Guillon, S. H. Song, H. Kim, H. D. Lim, H. G. Jung, Y. Kim, H. K. Lee, K. S. Lee, K. Yazawa, K. Gotoh, P. Kaghazchi, S. T. Myung, *Adv. Energy Mater.* **2022**, *12*, 2103939.
[32] E. De La Llave, P. K. Nayak, E. Levi, T. R. Penki, S. Bublil, P. Hartmann, F. F. Chesneau, M. Greenstein, L. F. Nazar, D. Aurbach, *J. Mater. Chem. A* **2017**, *5*, 5858.
[33] N. K. Karan, M. D. Slater, F. Dogan, D. Kim, C. S. Johnson, M. Balasubramanian, *J. Electrochem. Soc.* **2014**, *161*, A1107.
[34] J. Xu, D. H. Lee, R. J. Clément, X. Yu, M. Leskes, A. J. Pell, G. Pintacuda, X.-Q. Yang, C. P. Grey, Y. S. Meng, *Chem. Mater.* **2014**, *26*, 1260.
[35] K. J. Zhou, A. Walters, M. Garcia-Fernandez, T. Rice, M. Hand, A. Nag, J. Li, S. Agrestini, P. Garland, H. Wang, S. Alcock, I. Nistea, B. Nutter, N. Rubies, G. Knap, M. Gaughran, F. Yuan, P. Chang, J. Emmins, G. Howell, *J. Synchrotron Radiat.* **2022**, *29*, 563.